Energies **2015**, *8*, 6608-6626; doi:10.3390/en8076608

OPEN ACCESS

energies

ISSN 1996-1073

www.mdpi.com/journal/energies

Article

Development of an Axial Flux MEMS BLDC Micromotor with Increased Efficiency and Power Density

Xiaofeng Ding [1], Guanliang Liu [1,†], Min Du [1,†], Hong Guo [1], Hao Qiao [1,*] and Christopher Gerada [2]

[1] School of Automation Science and Electrical Engineering, Beihang University, Beijing 100191, China; E-Mails: dingxiaofeng@buaa.edu.cn (X.D.); liu_guanliang@163.com (G.L.); dumin0201@gmail.com (M.D.); guohong@buaa.edu.cn (H.G.)

[2] Department of Electrical and Electronic Engineering, the University of Nottingham, Nottingham NG7 2RD, UK; E-Mail: Chris.Gerada@nottingham.ac.uk

† These authors contributed equally to this work.

* Author to whom correspondence should be addressed; E-Mail: qianhao@buaa.edu.cn; Tel./Fax: +86-10-8233-8455.

Academic Editor: Paul Stewart

Received: 2 April 2015 / Accepted: 27 May 2015 / Published: 30 June 2015

Abstract: This paper presents a rigorous design and optimization of an axial flux microelectromechanical systems (MEMS) brushless dc (BLDC) micromotor with dual rotor improving both efficiency and power density with an external diameter of only around 10 mm. The stator is made of two layers of windings by MEMS technology. The rotor is developed by film permanent magnets assembled over the rotor yoke. The characteristics of the MEMS micromotor are analyzed and modeled through a 3-D magnetic equivalent circuit (MEC) taking the leakage flux and fringing effect into account. Such a model yields a relatively accurate prediction of the flux in the air gap, back electromotive force (EMF) and electromagnetic torque, whilst being computationally efficient. Based on 3-D MEC model the multi-objective firefly algorithm (MOFA) is developed for the optimal design of this special machine. Both 3-D finite element (FE) simulation and experiments are employed to validate the MEC model and MOFA optimization design.

Keywords: axial flux; microelectromechanical system (MEMS); efficiency; power density; magnetic equivalent circuit (MEC); multi-objective firefly algorithm (MOFA)

1. Introduction

Micromotors are indispensable for driving microelectromechanical systems (MEMS). There are many types of micromotors, such as electrostatic, piezoelectric and electromagnetic ones. Due to the fact that MEMS evolved from microelectronic technology, most of the prior literature is focused on electrostatic micromotors [1]. Recently, electromagnetic micromotors with a larger torque capability than electrostatic and piezoelectric mircomotors have attracted lots of attention.

Electromagnetic motors at the MEMS scale have not been systematically explored. The first electromagnetic systems assembled with permanent magnets were reported in 2006 [2]. Rare earth magnets such as neodymium-iron-boron (NdFeB) are often used in these micromotors to provide for high energy density. This also indicates that some these machines are often heavily thermally loaded. Given the micro dimensions of these devices, they are susceptible to excessive temperature rises, which in turn degrades the performance and may cause irreversible demagnetization of the magnets [3]. The special windings adopted in these machines are also susceptible to temperature, potentially leading to fusing failures.

In real practice, the output torque of a micromotor is always limited by the thermal load. In reference [1], a micromotor was designed with special emphasis on the maximization of its efficiency. The Joule efficiency obtained is about 42%, which is much higher than those reported for electromagnetic MEMS micromotors [4,5]. However, the capability of its output torque is only 3.78 nNm due to its micro dimensions (external diameter is 2.6 mm). For real applications, such as microrobotics and microaircraft to be competitive, micromotors need to simultaneously have a high output torque density and high efficiency.

Hence, the design of micromotors is typically a nonlinear, multi-objective, optimization problem. Different objectives often conflict with each other, and sometimes a truly optimal solution does not exist. Design compromise and approximation are often needed [6]. Metaheuristic algorithms are very powerful in dealing with this kind of optimization problem [7–11]. The firefly algorithm (FA) is one of the Nature-inspired metaheuristic algorithms proposed by Yang at Cambridge University in 2008 [7]. Multiobjective FA (MOFA) was further developed by Xin-She Yang later in 2012 [11]. Such a multiobjective algorithm is powerful in dealing with design problems in electrical machines with a large number of design variables and multiple objectives under complex nonlinear constraints. Therefore, this paper proposes such an algorithm as a tool for optimizing the design of a micromotor first time.

The remainder of this paper is organized as follows: a description of the axial flux MEMS BLDC micromotor is presented in Section 2. The analytical modeling of the micromotor is developed in Section 3. The stator fabrication following almost-standard MEMS technology is introduced in Section 4. The MOFA optimization for the design of the micromotor targeting both power density and efficiency improvement is presented in Section 5. 3D FEA simulation and experimental verification is reported in Section 6. Conclusions are drawn in Section 7.

2. Basic Structure and Operation Principle

2.1. The Micromotor Structure

Figure 1 shows the basic structure of an axial flux MEMS micromotor in an exploded geometry view. The stator coils are manufactured on a silicon wafer by a deep etching process, which is standard MEMS technology. The permanent magnets (PMs) with ring shape are assembled over the rotor yokes. The two rotors are symmetrically distributed on two sides of the stator, which improves the output torque as well as avoids any one-sided asymmetric magnetic forces [12]. Furthermore, the stator without the iron core benefits from no iron loss. The surface mounted coils can operate at relatively high current density as they are exposed to a good air flow as the rotor rotates.

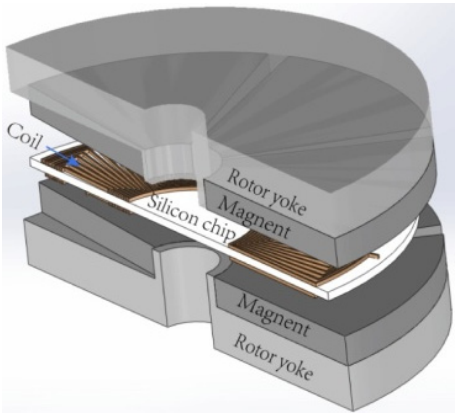

Figure 1. The structure of an axial-flux MEMS micromotor.

In this paper the motor prototype has three phases and 18 coils in total will be shown later. It means that there are six coilsper phase connected in series. Nine coils are distributed symmetrically over each side of the silicon wafer. The upper side coils and corresponding back side coils are connected through via-holes. The three phases are connected in Y topology. The distribution of three phases is shown in Figure 2. Phases A, B and C are distributed counterclockwise. Figure 2 also shows the distribution of the PMs. The PMs are axially magnetized simultaneously. Such a magnetization method leads to a good magnetization field distribution. The rotor consists of three pairs of magnetic poles distributed as shown in Figure 2. In order to avoid excessive flux leakage, the pole-arc coefficient is smaller than 100% [13–15].

2.2. Operation Principle

The operation principle of the micromotor is described in Figure 2. The stator and the rotor on one side of the motor are visible. The other side moves synchronously with the upper side. The magnetizing direction is axial. ⊗ denotes that the magnetic field is orientated in the direction perpendicular to the page pointing inward. ⊙ represents the magnetic field oriented in the direction pointing outwards perpendicular to the page.

Due to the micro dimension of the machine, there is not enough space for assembling any position sensors, such as Hall sensors or resolvers. Therefore, the motor is driven via a senorless approach. During startup, the motor is initially idle and has no back EMF to synchronize the commutator loop.

In order to get sufficient back EMF to close the loop, it is necessary to start the motor in open loop. Figure 2a shows the motor startup stage. Currents of phase A and C flow in the clockwise direction, while current of phase B flows in the counterclockwise direction. Then the rotor will be aligned into the position shown in Figure 2a according to the right-hand rule.

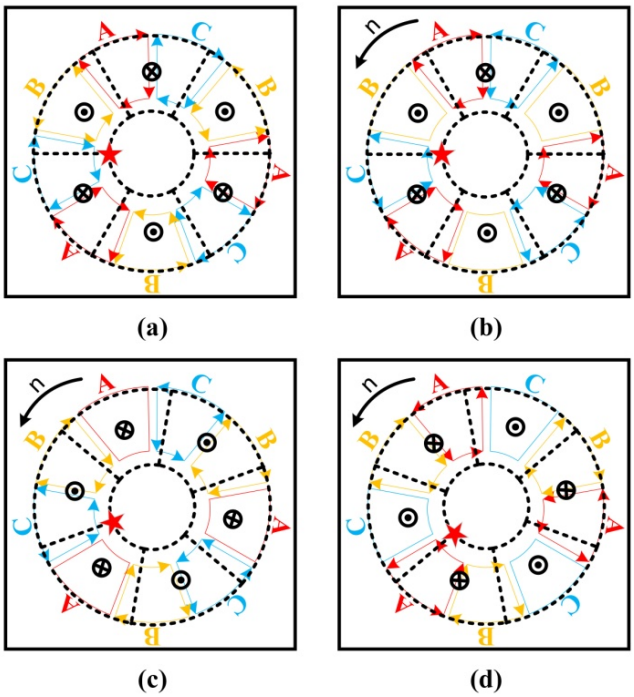

Figure 2. Schematic diagram of the interaction between the stator and rotor windings. (**a**) The initial position; (**b**) 0° electrical angle position; (**c**) 60° electrical angle position; (**d**) 120° electrical angle position.

At the end of the alignment mode the motor goes into a speed ramping mode. When the back EMF is sufficient the motor will enter the closed-loop running mode. The three-phase voltages are shown in Figure 3. The current flows in the clockwise direction shown in Figure 2 corresponding to the positive voltage shown in Figure 3. When the rotor arrives at the 0° electrical angle as shown in Figure 2b, the current of phase A flows in the clockwise direction while the current of phase C flows in the counterclockwise direction, which depends on the supply voltages of phase A and C at T0 shown in Figure 3. Therefore, the radial conductors of the windings are attracted by the clockwise electromagnetic force due to the magnetic field induced by the PMs of the rotor. In turn, the rotor is attracted by the opposite force, thereby rotating in the counterclockwise direction as shown in Figure 2b. When the rotor reaches a 60° electrical angle as shown in Figure 2c, the current of phase C still flows in the counterclockwise direction. The current of phase A disappears and the current of phase B starts to flow in the clockwise direction. Such currents depend on the voltages of phase B and C at T1 shown in Figure 3. Therefore, the rotor is attracted by a counterclockwise electromagnetic force as well. Such a rotation mechanism is also suitable for the rotor moving to the position shown in Figure 2d. Hence, the rotor rotates continuously in the counterclockwise direction by the corresponding electromagnetic force. The movement of the rotor is demonstrated by a red star ★ shown in Figure 2.

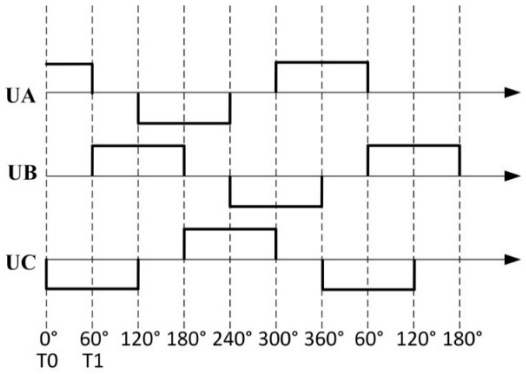

Figure 3. Supply voltage waveforms of the three phases.

3. Analytical Modeling

A set of equations describing the motor from basic electromagnetic principles are developed. Such equations are used for the optimization design of the micromotor to enhance both the power density and efficiency. In order to simplify the calculation, modeling of the MEMS motor is based on some assumptions as follows:

- There is no saturation occurring in the rotor yokes;
- The magnetic field intensity produced by the armature current in the stator windings is negligible;
- The reluctances of the rotor yokes are neglected.

3.1. Flux Density in Air Gap

The flux density in the air gap generated by the permanent magnets is critical for developing the analytical model. Figure 4a shows the magnetic circuit of the micromotor topology. Magnet-to-rotor and magnet-to-magnet leakage flux is pictured by blue and green lines, respectively, with the main-loop flux in red. A fringing effect exists at the external and internal radius of the magnets, as shown in Figure 4b. The circular-arc straight-line permeance model is used for modeling the flux flow in the air gap [13,14]. The reluctances of magnet to rotorR_{mr} and magnet to magnetR_{mm} are calculated taking the radial length of magnets in 3D space into account. The tangential length of magnets is considered when calculating fringing reluctances R_e and R_i. All the above reluctances can be expressed as Equations (1)–(4). The equivalent magnet circuit is proposed in Figure 5.

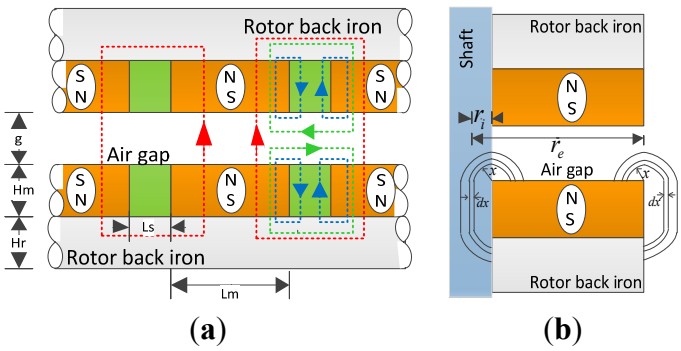

Figure 4. Magnetic loop of the axial-flux micromotor. (**a**) Leakage fluxes; (**b**) Fringing effect.

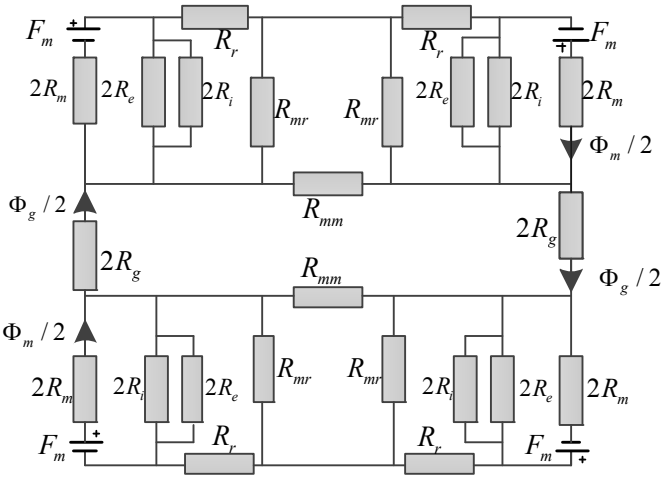

Figure 5. Equivalent magnetic lumped circuit for Figure 4.

$$R_{mr} = 1/[\frac{1}{L_e - L_i}(\int_{L_i}^{L_e} dL_s \int_0^{\frac{L_s}{2}} \frac{\mu_0 L}{H_m + \pi x} dx)] = 1/\{\frac{1}{L_e - L_i}[\int_{L_i}^{L_e} \frac{\mu_0 L}{\pi} \ln(1 + \frac{\pi L_s}{2H_m}) dL_s]\} \quad (1)$$

$$R_{mm} = 1/[\frac{1}{L_e - L_i}(\int_{L_i}^{L_e} dL_s \int_0^{\frac{L_s}{2}} \frac{\mu_0 L}{L_s + \pi x} dx)] = 1/\{\frac{1}{L_e - L_i}[\int_{L_i}^{L_e} \frac{\mu_0 L}{\pi} \ln(1 + \frac{\pi g}{2L_s}) dL_s]\} \quad (2)$$

$$R_e = 1/(\int_0^y \frac{\mu_0 L_{em}}{H_m + \frac{3}{2}\pi x} dx) = 1/[\frac{\mu_0 L_{em}}{\frac{3}{2}\pi} \ln\left(1 + \frac{3\pi y}{2H_m}\right)] \quad (3)$$

$$R_i = 1/(\int_0^y \frac{\mu_0 L_{im}}{H_m + \frac{3}{2}\pi x} dx) = 1/[\frac{\mu_0 L_{im}}{\frac{3}{2}\pi} \ln\left(1 + \frac{3\pi y}{2H_m}\right)] \quad (4)$$

$$F_m = H_c H_m = \frac{B_r H_m}{\mu_0 \mu_r} \quad (5)$$

$$R_g = \int_{L_{s_{min}}}^{L_{s_{max}}} \frac{g}{\mu_0 L_s L} dL_s \quad (6)$$

where, $L_{em} = \theta \cdot r_g$, $L_{im} = \theta \cdot r_g$ and $L = r_g - r_i$, θ is the radian of one magnet, $L_g = (\frac{\pi}{P} - \theta) \cdot r_g$, $L_i = (\frac{\pi}{P} - \theta) \cdot r_i$, and P is the number of pole pairs. The variable y depends on the motor dimension and the magnetic material properties. F_m, R_g and R_r represent the equivalent magnetomotive force source, reluctance corresponding to Φ_g and reluctance of the rotor back iron, respectively. The above equivalent magnetic lumped circuit can be simplified to give the following circuit in the Figure 6:

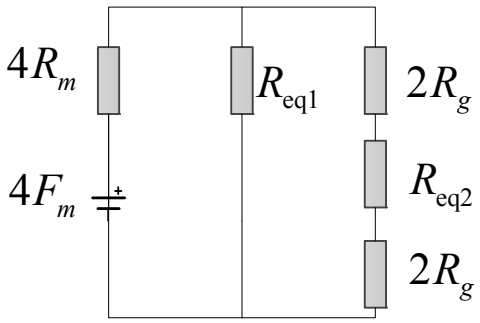

Figure 6. Simplified equivalent magnetic lumped circuit.

R_{eq1} and R_{eq2} represent the equivalent resistances, which are shown as follows:

$$\frac{1}{R_{eq1}} = \frac{1}{4R_i} + \frac{1}{4R_e} + \frac{1}{2R_{mr}} + \frac{1}{R_{mm}} \tag{7}$$

$$\frac{1}{R_{eq1}} = \frac{1}{4R_i} + \frac{1}{4R_e} + \frac{1}{2R_{mr}} + \frac{1}{R_{mm}} + \frac{1}{4R_m} \tag{8}$$

According to the circuit theorem, magnetic flux density of the air gap can be obtained as:

$$\varphi_g = \frac{4R_g}{4R_g + R_{eq2}} \times \frac{R_{eq3}}{R_{eq3} + 4R_m} \times 4F_m \tag{9}$$

$$\frac{1}{R_{eq3}} = \frac{1}{R_{eq1}} + \frac{1}{4R_g + R_{eq2}} \tag{10}$$

$$B_g = \frac{\varphi_g}{S_g} \tag{11}$$

$$S_g = \frac{(L_{em} - 2L_e) \times r_e - (L_{im} - 2L_i) \times r_i}{2} \tag{12}$$

where φ_g represents the flux in the air gap, calculated by the circuit theorem in the formula Equation (9). B_g is the flux density in the air gap, defined as Equation (11). s_g is the effective area of the air gap. The effective area is defined as the entire upper surface of the magnet after subtracting the area of the leakage flux. The flux density is assumed as sinusoidally distributed along the circumferential direction in the air gap. The d-axis is defined as 0° electrical angle. The flux density in any electrical angle is:

$$B = B_\delta cos\theta \tag{13}$$

3.2. Back EMF

Due to the small ratio of air-gap over motor radius, it is reasonable to assume that the axial flux density is constant and the radial flux is 0. One coil of the micromotor is shown in Figure 7. The cross-section of one layer is described in Figure 8. The red parts are conductors and the white parts are insulators. The back EMF of one conductor could be expressed as:

$$\varepsilon_i = \int_{r_{1i}}^{r_{2i}} B_\delta cos\theta_i \omega r dr = \frac{1}{2} B_\delta cos\theta_i \omega (r_{2i}^2 - r_{1i}^2) \tag{14}$$

where:

ε_i back EMF of conductor i;
r_{1i} internal radius of turn i;
r_{2i} external radius of turn i;
θ_i the electrical angle of conductor i;
i *=0,1,2,3…k-1*;
k the number of turns in one coil;
ω rotation angle velocity.

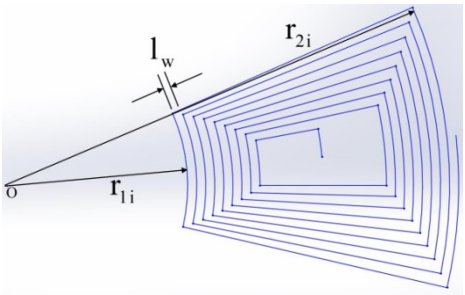

Figure 7. One coil structure of the micromotor.

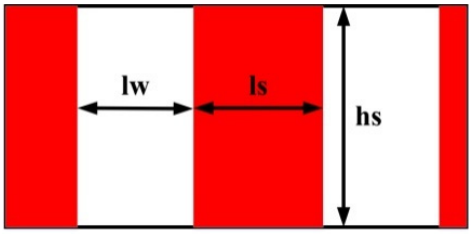

Figure 8. The cross-section of one layer of conductors.

Since there are *k* turns per coil, the back EMF of one coil is derived as:

$$\varepsilon = \frac{1}{2}\omega B_\delta \sum_{i=0}^{k-1}\left[cos\left(-\frac{\theta}{2}+\Delta\theta\cdot i\right)\cdot(r_{2i}^2-r_{1i}^2)+cos\left(\frac{\theta}{2}-\Delta\theta\cdot i\right)\cdot(r_{2i}^2-r_{1i}^2)\right] \quad (15)$$

where:

k the number of turns in one coil;
θ $= \frac{P\cdot 2\pi}{n}$ radian of one coil;
P number of pole pairs;
n number of coils on one side of silicon wafer;
$\Delta\theta$ $= p\cdot\frac{l_w}{(r_1+r_2)/2}$;
l_w insulator width;
r_1 external radius of coil;
r_2 internal radius of coil.

The motor has three phases and *2n* coils in total, which means that there are *2n/3* coils per phase connected in series. The back EMF of one phase is:

$$E_\theta = \frac{n}{3}\omega B_\delta \sum_{i=0}^{k-1}[cos\left(-\frac{\theta}{2} + \Delta\theta \cdot i\right) \cdot (r_{2i}^2 - r_{1i}^2) + cos\left(\frac{\theta}{2} - \Delta\theta \cdot i\right) \cdot (r_{2i}^2 - r_{1i}^2)] \quad (16)$$

3.3. Average Output Torque

The average back EMF of one phase is:

$$\bar{E} = \frac{\int_{\theta_{starting}}^{\theta_{end}} E_\theta d\theta}{2\pi/3} \quad (17)$$

where $\theta_{starting} = \theta_{max} - \frac{p\pi}{n}$, $\theta_{starting} = \theta_{max} + \frac{p\pi}{n}$. The average back EMF reach the maximum value at $\theta = \theta_{max}$, shown as below:

$$\bar{E} = -\frac{n}{2\pi}\omega B_\delta \sum_{i=0}^{k-1}(r_{2i}^2 - r_{1i}^2)[sin\left(\theta_{max} + \frac{p\pi}{n} - \frac{\theta_i}{k}\right) - sin\left(\theta_{max} - \frac{p\pi}{n} + \frac{\theta_i}{k}\right)] \quad (18)$$

Small value of inductances is negligible [9]. Therefore, current of phase is given as below:

$$I = \frac{U - 2\Delta U - 2\bar{E}}{2R} \quad (19)$$

Here U is the power voltage, ΔU is voltage drop across one MOSFET, R is resistance of one phase. The electromagnetic torque could be calculated as:

$$\bar{T} = \frac{2\bar{E}I}{\omega} \quad (20)$$

3.4. Joule Efficiency of Motor

In order to calculate the joule efficiency of the motor, the phase resistance is developed as:

$$R_{ph} = \rho_{cu}\frac{\sum_{i=0}^{k-1} l_i}{l_s \cdot h_s} \quad (21)$$

Here h_s is height of the conductor, l_s is width of the conductor and l_i is length of turn i given as:

$$l_i = 2(r_{2i} - r_{1i}) + r_{1i} \cdot (\theta - i \cdot \Delta\theta) + r_{2i} \cdot (\theta - i \cdot \Delta\theta) \quad (22)$$

Here, $r_{1i} = r_1 + i \cdot l_w, r_{2i} = r_2 - i \cdot l_w$.

Since at any moment there are two phases conducting, the Joule losses of the whole motor can be computed as:

$$P_J = 2P_{J,ph} = 2R_{ph} \cdot I_{ph,rms}^2 \quad (23)$$

Therefore, the Joule efficiency of the motor is:

$$\eta_J = \frac{P_{emc}}{P_{emc} + P_J} \quad (24)$$

4. Model Validation by FEA Simulations and Experiments

In this section, the analytical model developed previously is verified by both FEA simulation and experiments. Conventional PCB technology is relatively mature. The manufacturing process is relatively simple and the production costs are low. Therefore, in order to carry out experiments to validate the analytical model of the machine, the micromotor is assembled with the stator based on PCB manufacturing technology. The 3D FE model of the motor is developed in MAXWELL software with the PCB stator shown in Figure 9. There are only five turns per coil due to the limitation imposed by the PCB manufacturing technology. The minimal width of conductor is 0.1 mm, while the minimal width of the conductor could be manufactured to the scale of several μm via MEMS. A comparison between PCB and MEMS is described in Section 4. The PCB stator prototype is shown in Figure 10 with parameters of this micromotor listed in Table 1.

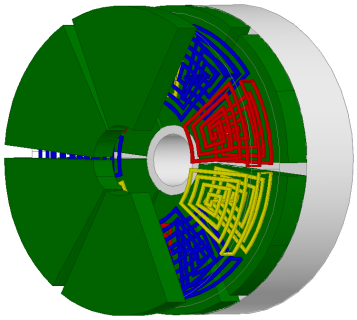

Figure 9. 3D axial flux micromotor with PCB stator.

Figure 10. PCB stator.

Table 1. Specifications of the micromotor.

Parameter	Symbol	Value
Rated current (A)	i	0.1
Rated speed (rpm)	n	20,000
Stator external diameter (mm)	r_e	9.5
Stator internal diameter (mm)	r_i	2.5
Magnet height (mm)	H_m	0.75
Magnet pole arc ratio	-	0.85
Rotor back iron height (mm)	H_r	1.5
Air-gap length (mm)	g	1.6
Pole pairs	p	3

Figure 11 shows the back EMFs obtained from the analytical calculation, FE simulation and experiments, respectively, which show a good match. Other electromagnetic variables are also validated as shown in Table 2. In the worst situation, the error between the analytical model and the experiments is lower than 10%, which also verifies that the analytical model is accurate enough for the motor design optimization.

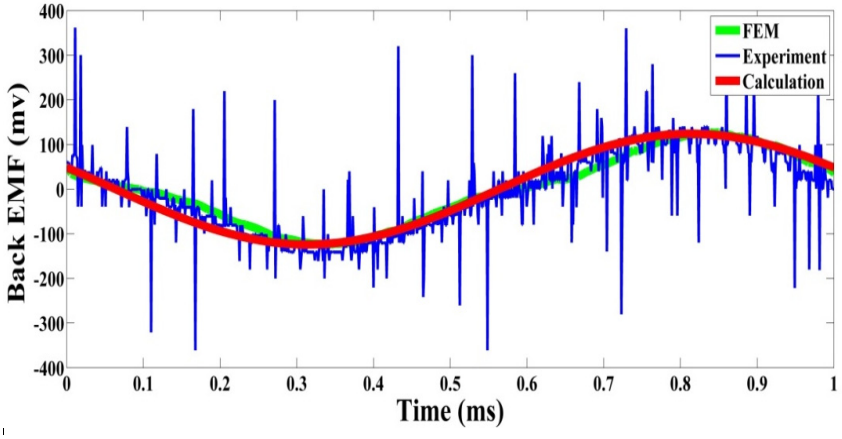

Figure 11. Back EMFs of the micromotor from experiments, FEM and analytical calculations.

Table 2. Comparison between the results obtained with the analytical model and simulations.

Physical Variable	Analytical Model	FEA	Experiment
Flux density, B_δ (T)	0.5797	0.59	-
Torque, T (μNm)	9.68	9.89	10.25
Back EMF, E (mV)	122	128	130.5

5. Stator Fabrication

Due to the complex MEMS technology manufacturing process, one stator based on a printed circuit board (PCB) is manufactured and assembled in the prototype micromotor instead of the MEMS stator, which was already presented in Section 3. However, the PCB technology is not suitable for the miniaturization of the micromotor. The minimum width of the copper conductor-based PCB is limited to 0.1 mm. If the width of conductor is 0.1 mm, the maximum height of the conductor is only stacked to 0.1 mm. The ratio of height over width ratio is 1. On the other hand, the minimum width of a copper conductor based on MEMS is less than 10 μm and ratio of height over width ratio is more than 8. The smaller the width of the conductor, the more coils are to be manufactured on the same silicon wafer, which means a higher amplitude of the back EMF and thereby higher output torque. In addition, the higher height over width ratio results in a higher current density of the conductor. Therefore, the output torque is further enhanced by the increment of the current. A comparison between PCB and MEMS technology is shown in Table 3.

Table 3. Comparison between PCB and MEMS.

Parameters	PCB	MEMS
Min width of conductor	0.1 mm	Less than 10 μm
Max height of conductor	0.1 mm	More than 80 μm
Insulator	0.1 mm	Less than 10 μm

Given the advantage of MEMS technology this paper develops a stator based on it. The process flow, which includes more than 20 steps, is quite complicated and time consuming. A simplified version is shown in Figure 12 and described as below.

Step 1: The fabrication starts from a silicon wafer with thickness of 400 μm and a 4 μm silicon oxide (SiO_2) layer. Then spin coating, prebaking, exposure and development of the silicon wafer are implemented in sequence (Figure 12a). The prebaking temperature affects the exposure and development performances directly, so a suitable temperature of 115 °C is selected based on the experimental results;

Step 2: The silicon wafer is baked via a hot plate. The exposed SiO_2 layer is etched off via hydrofluoric (HF) acid (Figure 12b);

Step 3: Grooves with width of 42 μm and depth of 80 μm are etched on the slicon wafer by an ALCATEL601E inductively coupled plasma etcher (ICP) (Figure 12c). Photoresist and SiO_2 are used as a hard mask;

Step 4: A 1 μm aluminum (Al) layer is sputtered over the upper surface of the silicon wafer. Then spin coating, exposure, development and etch are carried out on this surface. The holes are etched in the ICP again after stripping of photoresist (Figure 12d) Al is used to protect the upper surface of the silicon wafer while the down surface is in the fabrication stage. The fabrication process of the down surface is the same as the upper side, therefore only the upper side process is described;

Step 5: A complete silicon groove structure is formed after removing the aluminum cover. After a wet oxidation of the grooves to prevent any short circuits via the silicon substrate, a copper (Cu) seed layer with 200 nm thickness is sputtered over the whole wafer surface (Figure 12e);

Step 6: After a second photolithography and etch, only the cooper seed layer in the grooves is left (Figure 12f);

Step 7: Finally these grooves are filled with the electroplated copper to create the metal lines of the windings (Figure 12g).

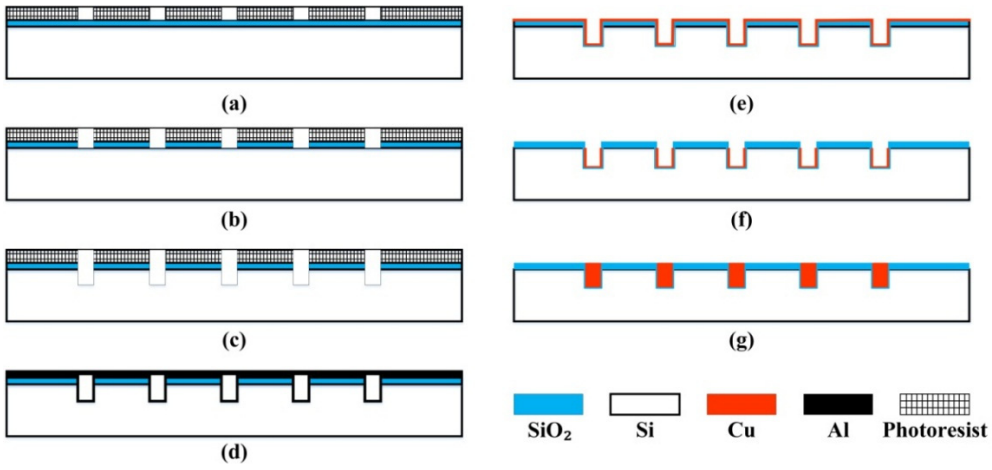

Figure 12. Scheme of the MEMS processing flow. (**a**) silicon wafer with SiO2; (**b**) silicon wafer without portion of SiO2; (**c**) silicon wafer with grooves; (**d**) silicon wafer with Al layer; (**e**) silicon wafer with a wet oxidation of the grooves; (**f**) silicon wafer with the cooper seed layer in the grooves; (**g**) silicon wafer with the metal lines of the windings.

6. Firefly Algorithm-Based Design Optimization

The FA is one of the Nature-inspired metaheuristic algorithms. The inspiration comes from the flashing light of the firefly. Though the true functions of such signaling systems are still being debated, two fundamental functions of such flashes are to attract mating partners (communication) and potential prey. Based on the flashing characteristics of fireflies the novel firefly algorithm was developed by Xin-She Yang at Cambridge University [7,9–11]. Such an algorithm is powerful in dealing with design problems of electrical machines with a large number of design variables and multiple objectives, under complex nonlinear constraints. Therefore, in this paper the MOFA is used to optimize this special micromotor for the first time. Six design variables are shown in Table 4. The geometry constraints and operating limits are shown in Table 5. Current is fixed as 0.1A according to the cooling conditions.

Table 4. Design Variables and Ranges.

Variables	Range	Unit
Stator external diameter	[6~15]	mm
Magnet height	[0.5~2.2]	mm
Number of coils	[6~15]	
Conductor width	[0.04~0.06]	mm
Insulator width	[0.02~0.04]	mm
Power voltage	[1~1.5]	V

Table 5. Design Constraints.

Variables	Value	Unit
Rated current	≤0.1	A
Rated speed	20,000	rpm
Pole pairs	3	
Torque	>35	μNm
Air-gap length (mm)	1.5	mm
Stator internal diameter (mm)	3	mm

The optimization process is described as follows. Firstly, the firefly population is randomly scattered in the solution space. Every firefly emits a distinct brightness light due to its different location. High brightness fireflies can attract low brightness fireflies moving towards them. The distances moved depend on the level of attractiveness. In order to increase the search area and avoid any premature local optimum, the updated location is calculated with an injected disturbance. After moving many times, all individuals will gather at the position of the highest firefly brightness. Hence the optimization results are obtained. The MOFA implementation is based on the following steps:

Step 1: Initialize the numbers of fireflies n, biggest attraction β_0, absorption coefficient of light intensity γ, step size factor α, and maximum of iterations or generations t_{max}.

Step 2: Initialize the positions of fireflies randomly, namely initializing design variables of the machine, the values of objective functions of fireflies are set as their maximum brightness of fluorescence I_o.

Step 3: Calculate relative brightness and attractiveness of fireflies, which belong to the population. The direction of movement depends on the relative brightness of fireflies. Here:

$$I = I_0 \times e^{-\gamma r_{ij}} \tag{25}$$

$$\beta = \beta_0 \times e^{-\gamma r_{ij}} \tag{26}$$

where I_0 is the maximum fluorescence brightness of the firefly, namely the fluorescence brightness itself (r = 0), which depends on the value of the objective function. β_0 is the maximum attractiveness, namely the attractiveness of the light source (r = 0). γ is the absorption coefficient of the light intensity. The fluorescence will gradually weaken according to the increasing distance and the absorption of media. The absorption coefficient of light intensity is set to reflect this feature. r_{ig} is the spatial distance between firefly i and j.

Step 4: Update the spatial positions of fireflies. Random perturbations are injected to the firefly with the best position. The updated equation is:

$$x_i = x_i + \beta \times (x_j - x_i) + \alpha \times (rand - 0.5) \tag{27}$$

where x_i, x_j represent the spatial positions of firefly i and j, respectively. α is step size factor. $rand$ is random factor distributed uniformly in [0,1].

Step 5: Recalculate the brightness of fireflies according to the updated positions.

Step 6: Return to Step 3 until the search precision is met or the maximum number of generations is achieved.

The proposed optimal design is checked by making a comparison between the reference motor and optimized motor shown in Table 6. Although the dimensions of the machine increase slightly from 367.43 to 439.12 mm^3, the improvement of power density T/V is almost 6 Nm/m^3. In addition, the increment of the efficiency is more than 8%.

Table 6. Optimization results.

Variables Comparison	**Reference**	**MOFA**
Number of coils	9	9
Stator external diameter (mm)	9.6	10.2
PM thickness (mm)	0.8	0.88
Insulator width (mm)	0.04	0.042
Conductor width (mm)	0.04	0.038
Power voltage (V)	1.26	1.5
Performance Comparison	**Reference**	**MOFA**
Dimension (mm^3)	367.43	439.12
Torque ($\mu N \cdot m$)	32.1	40.97
T/V (Nm/m^3)	87.4	93.3
Efficiency	0.53	0.573

7. 3D FEA Simulation and Experimental Verification

In this section, the optimized design of the machine is verified by both 3D FEA simulation and experiments.

7.1. 3D FEA Simulation Verification

Figure 13 shows the 3D axial flux micromotor with the MEMS stator developed in the MAXWELL software. To demonstrate the improvement of the optimized micromotor, a comparison between the reference and the optimized one is implemented via simulation. The waveforms of the back EMF of the two micromotors are shown in Figure 14. The amplitude of the reference one is 372 mV shown in Figure 14a, while the amplitude of the optimized micromotor reaches up to 450 mV shown in Figure 14b. The increment is more than 77 mV, which is remarkable improvement for the micromotor. Based on the same values of the phase current, the increment of the back EMF represents the increase of electromagnetic torque output. The electromagnetic torque is rising from 32.8 to 41.4 μN · m shown in Figure 15a,b respectively. And the other benefit is given that the torque ripple of the optimized one is smaller than the reference one according to the reasonable distribution of windings. Meanwhile, the efficiency rises from 52.3% to 56.9%. Hence, both efficiency and power density are improved and consistent with the results from MOFA analytical calculation.

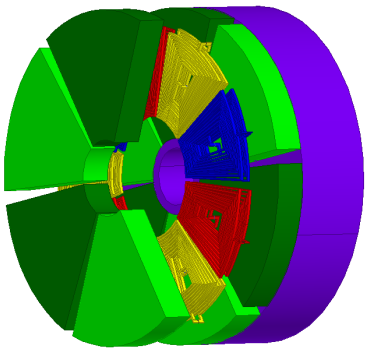

Figure 13. 3D axial flux micromotor with MEMS stator.

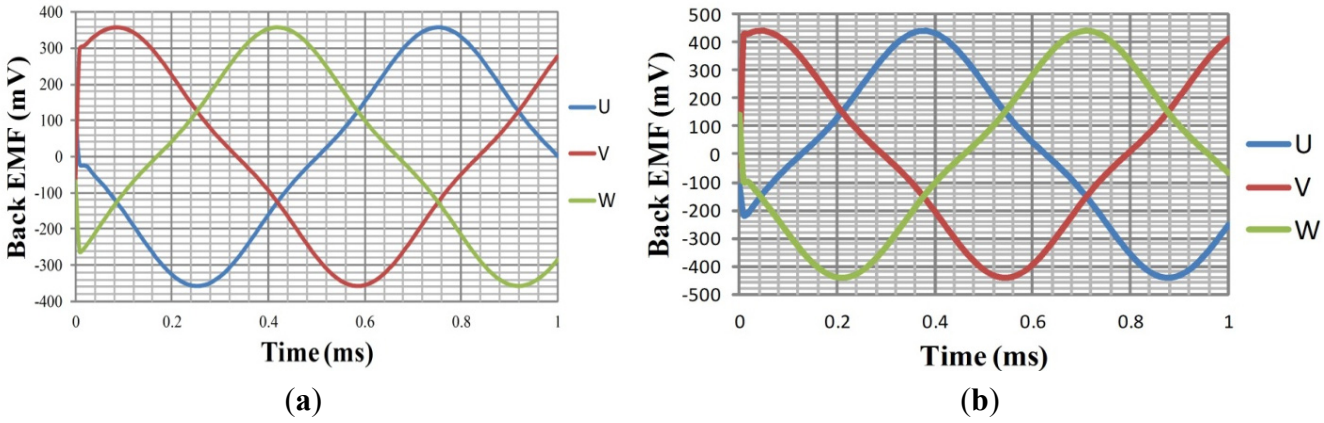

Figure 14. Back EMF waveforms of the two micromotors. (**a**) Back EMF of the reference micromotor; (**b**) Back EMF of the optimized micromotor.

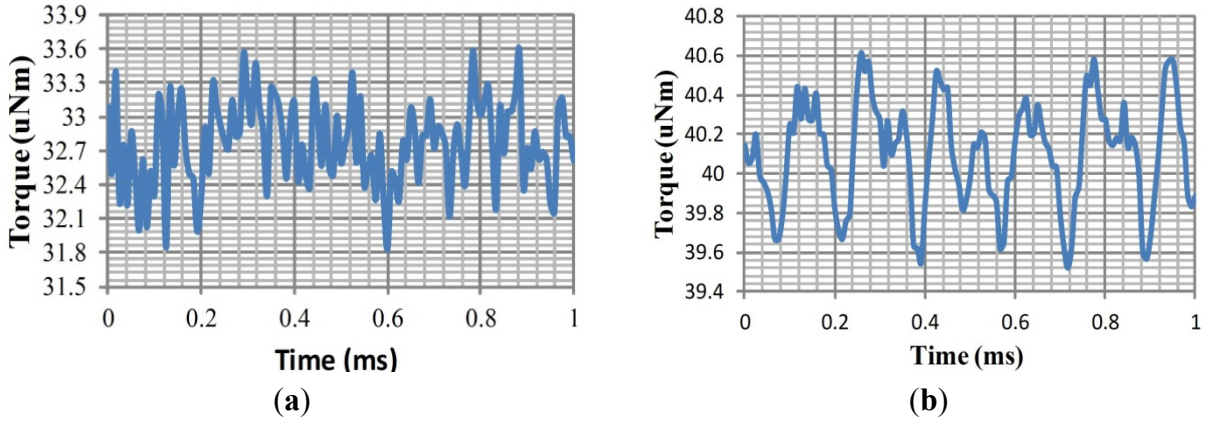

Figure 15. Electromagnetic torques of the two micromotors. (**a**) Electromagnetic torque of the reference micromotor; (**b**) Electromagnetic torque of the optimized micromotor.

7.2. Experimental Verification

A prototype is manufactured according to the optimization design shown in Figure 16a. The stator is fabricated on the silicon wafer in a clean room as described in Section 4. To demonstrate the micro dimensions of the machine, a coin is compared with it as shown in Figure 16b. The diameter of the coin is 19.5 mm. The experimental bench of the MEMS micromotor is shown in Figure 17. The driver is developed based on a sensorless BLDC drive chip ML4426.

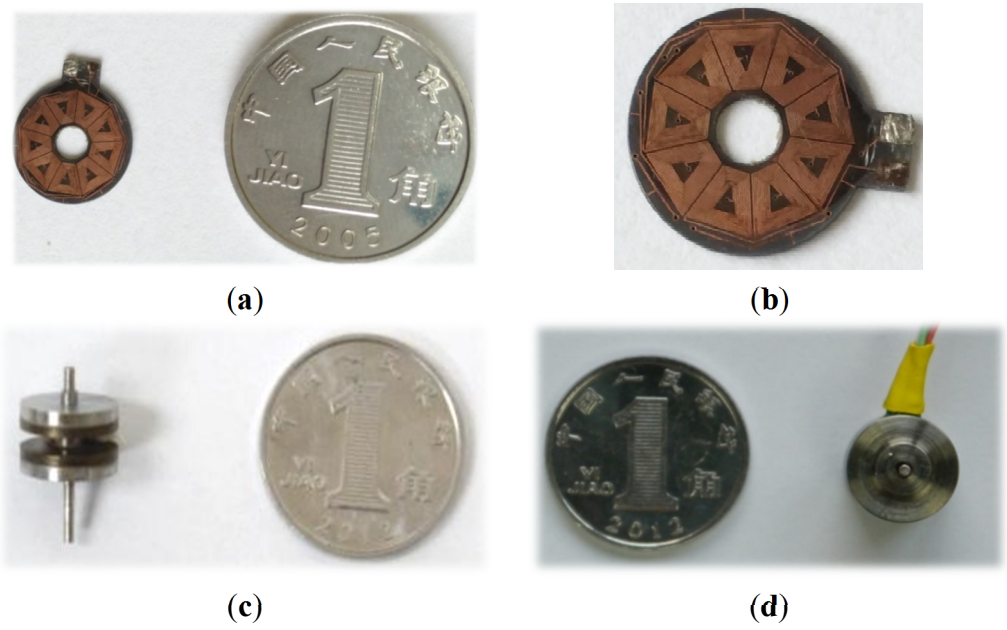

Figure 16. Prototype of MEMS micromotor. (**a**) stator; (**b**) stator with enlarged view; (**c**) dual rotor; (**d**) external view of the micromotor.

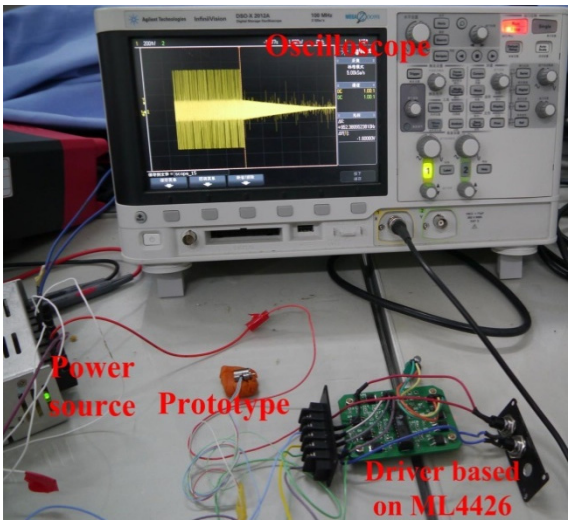

Figure 17. Experimental bench.

Figure 18 shows the PWM control signals for low side drive devices. The PWM duty cycle depends on the output power requirement. The back EMF of phase B is measured as shown in Figure 19. When the speed of the motor is 20,000 rpm the frequency of the back EMF is 1 kHz.

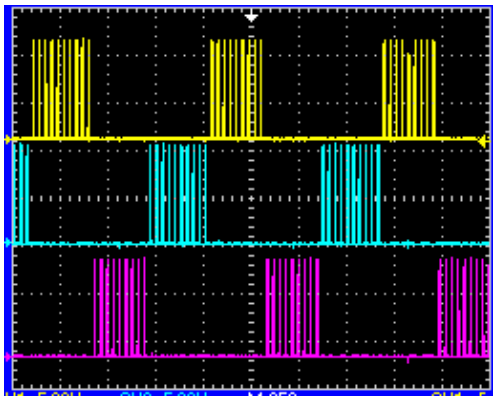

Figure 18. PWM control signals for low side drive devices.

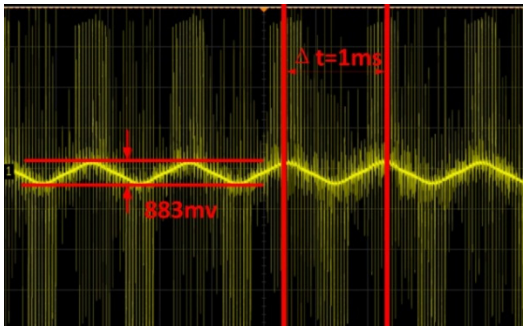

Figure 19. Back EMF of the micromotor @ 20,000 rpm.

The electromagnetic torque is difficult to measure due to the micro dimensions. Therefore a spin-down test is adopted. At a rated speed of 20,000 rpm, the electromagnetic torque is used to overcome the friction and windage torque only. Therefore, the friction and windage torque are equal to the electromagnetic torque. The waveforms of the back EMF during the spin-down of the micromotor

are shown in Figure 20. The motor rotational speed is computed as a function of the electric frequency of the back EMF. When the whole system inertia related to the rotor is given, the electromagnetic torque could be calculated as a function of the speed. In this paper, the estimated torque of the micromotor is 40.2 μN · m when the speed of the motor is 20,000 rpm, which is consistent with the simulation result and also validates the analytical calculations used during the MOFA optimization. The resulting efficiency is 56.5% as derived from the experiments. This demonstrates the validity of the modelling approach taken and the MOFA adopted.

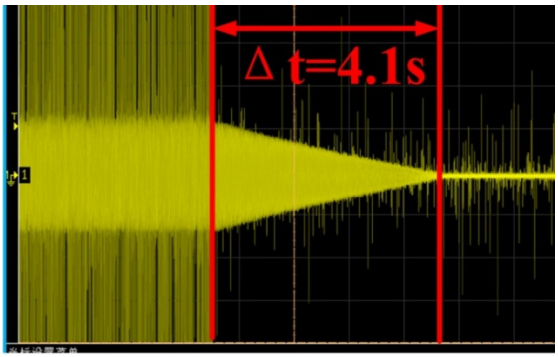

Figure 20. Back EMF measured during the rotor deceleration.

8. Conclusions

In this paper, an MEMS BLDC micromotor has been developed with improvement of both power density and efficiency. The diameter of the motor is only around 10 mm. Its stator is made of two layers with a high conductor height-over-width ratio, manufactured over a silicon wafer by a MEMS microfabrication process. The rotor is developed by ring shaped PMs assembled over the rotor yoke. A 3D MEC analytical model was developed and used for the optimization process. Such a model proved to be very valuable as it yields an accurate electromagnetic performance prediction of the micromotor as it takes the leakage flux and fringing effect into account. The MOFA is presented for the design optimization of the micromotor. The analytical model and MOFA optimization process for the micromotor are verified by both 3-D FE simulation and experiments. The improvement of power density is reflected in the improvement of torque-to-volume ratio of about 6 $\mathrm{Nm/m^3}$ and an increment of efficiency of about 8%. The optimally designed MEMS micromotor shows very good performance characteristics and demonstrates competitive potential for real applications at the MEMS scale.

Acknowledgments

This work was supported in part by the National Natural Science Foundation of China under Project 51407004 and in part by the Aeronautical Science Foundation of China 2013ZC51031.

Author Contributions

Xiaofeng Ding established the 3D MEC analytical model of the MEMS micromotor and performed the simulations with Hao Qian. Guanliang Liu implemented the MOFA optimization design. Min Du did the experiments and stator fabrication. Hong Guo provided some useful suggestions in the construction

of the paper framework. The paper was checked by Christopher Gerada. All authors carried out the theoretical analysis and contributed to writing the paper.

Conflicts of Interest

The authors declare no conflict of interest.

References

1. Merzaghi, S.; Koechli, C.; Perriard, Y. Development of a Hybrid MEMS BLDC Micromotor. *IEEE Trans. Ind. Appl.* **2011**, *47*, 3–11.
2. Achotte, N.; Gilles, P.-A.; Cugat, O.; Delamare, J.; Gaud, P.; Dieppedale, C. Planar brushless magnetic micromotors. *J. Microelectromech. Syst.* **2006**, *15*, 1001–1014.
3. Ding, X.F.; Mi, C. Modeling of Eddy Current Loss and Temperature of the Magnets in Permanent Magnet Machines. *J. Circ. Syst. Comput.* **2011**, *20*, 1287–1301.
4. Wagner, B.; Kreutzer, M.; Benecke, W. Permanent magnet micromotors on silicon substrates. *J. Microelectromech. Syst.* **1993**, *2*, 23–29.
5. Cros, F.; Koser, H.; Allen, M.; Lang, J. Magnetic induction micromachine—Part II: Fabrication and testing. *J. Microelectromech. Syst.* **2006**, *15*, 427–439.
6. Leifsson, L.; Koziel, S. Multi-fidelity design optimization of transonic airfoils using physics-based surrogate modeling and shape-preserving response prediction. *J. Comput. Sci.* **2010**, *1*, 98–106.
7. Yang, X.S. *Nature-Inspired Metaheuristic Algorithms*; Luniver Press: Beckington, UK, 2008.
8. Talbi, E.G. *Metaheuristics: From Design to Implementation*; Wiley: New York, NY, USA, 2009.
9. Yang, X.S. *Engineering Optimisation: An Introduction with Metaheuristic Applications*; Wiley: New York, NY, USA, 2010.
10. Yang, X.S. Firefly algorithms for multimodal optimization. *Stoch. Algorithms Found. Appl.* **2009**, *5792*, 169–178.
11. Yang, X.S. Multiobjective firefly algorithm for continuous optimization. *Eng. Comput.* **2013**, *29*, 175–184.
12. Mahmoudi, A.; Kahourzade, S.; Rahim, N.A.; Hew, W.P. Design, Analysis, and Prototyping of an Axial-Flux Permanent Magnet Motor Based on Genetic Algorithm and Finite-Element Analysis. *IEEE Trans. Magn.* **2013**, *49*, 1479–1492.
13. Ronghai, Q.; Lipo, T.A. Analysis and modeling of air-gap and zigzag leakage fluxes in a surface-mounted permanent-magnet Machine. *IEEE Trans. Ind. Appl.* **2004**, *40*, 121–127.
14. Huang, Y.; Zhou, T.; Dong, J.; Lin, H.; Yang, H.; Cheng, M. Magnetic Equivalent Circuit Modeling of Yokeless Axial Flux Permanent Magnet Machine with Segmented Armature. *IEEE Trans. Magn.* **2014**, *50*, 1–4.
15. Huang, Y.; Ge, B.; Dong, J.; Lin, H.; Zhu, J.; Guo, Y. 3-D Analytical Modeling of No-Load Magnetic Field of Ironless Axial Flux Permanent Magnet Machine. *IEEE Trans. Magn.* **2012**, *48*, 2929–2932.